Water vapour in the atmosphere of the habitable-zone eight-Earth-mass planet K2-18 b

Angelos Tsiaras [ID]*, Ingo P. Waldmann [ID]*, Giovanna Tinetti [ID], Jonathan Tennyson and Sergey N. Yurchenko

In the past decade, observations from space and the ground have found water to be the most abundant molecular species, after hydrogen, in the atmospheres of hot, gaseous extrasolar planets[1-5]. Being the main molecular carrier of oxygen, water is a tracer of the origin and the evolution mechanisms of planets. For temperate, terrestrial planets, the presence of water is of great importance as an indicator of habitable conditions. Being small and relatively cold, these planets and their atmospheres are the most challenging to observe, and therefore no atmospheric spectral signatures have so far been detected[6]. Super-Earths—planets lighter than ten Earth masses—around later-type stars may provide our first opportunity to study spectroscopically the characteristics of such planets, as they are best suited for transit observations. Here, we report the detection of a spectroscopic signature of water in the atmosphere of K2-18 b—a planet of eight Earth masses in the habitable zone of an M dwarf[7]—with high statistical confidence (Atmospheric Detectability Index[5] = 5.0, ~3.6σ (refs. [8,9])). In addition, the derived mean molecular weight suggests an atmosphere still containing some hydrogen. The observations were recorded with the Hubble Space Telescope/Wide Field Camera 3 and analysed with our dedicated, publicly available, algorithms[5,9]. Although the suitability of M dwarfs to host habitable worlds is still under discussion[10-13], K2-18 b offers an unprecedented opportunity to gain insight into the composition and climate of habitable-zone planets.

Atmospheric characterization of super-Earths is currently within reach of the Wide Field Camera 3 (WFC3) on board the Hubble Space Telescope (HST), combined with the recently implemented spatial scanning observational strategy[14]. The spectra of three hot transiting planets with radii less than 3.0 Earth radii ($R_\oplus$) have been published so far: Gliese 1214 b[15], HD 97658 b[16] and 55 Cancri e[17]. The first two do not show any evident transit depth modulation with wavelength, suggesting an atmosphere covered by thick clouds or made of molecular species heavier than hydrogen, while only the spectrum of 55 Cancri e has revealed a light-weight atmosphere, suggesting hydrogen–helium (H_2–He) still being present. In addition, transit observations of six temperate Earth-size planets around the ultra-cool dwarf TRAPPIST-1—planets b, c, d, e, f[5] and g[18]— have not shown any molecular signatures and have excluded the presence of cloud-free H_2–He atmospheres around them.

K2-18 b was discovered in 2015 by the Kepler spacecraft[7] and is orbiting around an M2.5 (metallicity [Fe/H] = 0.123 ± 0.157 dex (units of decimal exponent), effective temperature T_{eff} = 3,457 ± 39 K, stellar mass $M_\star$ = 0.359 ± 0.047 solar masses ($M_\odot$), stellar radius $R_\star$ = 0.411 ± 0.038 solar radii ($R_\odot$))[19] dwarf star, 34 pc away from the Earth. The star–planet distance of 0.1429 au (ref. [19]) suggests a

planet within the star's habitable zone (~0.12–0.25 au) (ref. [20]), with effective temperature between 200 K and 320 K, depending on the albedo and the emissivity of its surface and/or its atmosphere. This crude estimate accounts for neither possible tidal energy sources[21] nor atmospheric heat redistribution[11,13], which might be relevant for this planet. Measurements of the mass and the radius of K2-18 b (planetary mass M_p = 7.96 ± 1.91 Earth masses ($M_\oplus$) (ref. [22]), planetary radius R_p = 2.279 ± 0.0026 $R_\oplus$ (ref. [19])) yield a bulk density of 3.3 ± 1.2 g cm^{-1} (ref. [22]), suggesting either a silicate planet with an extended atmosphere or an interior composition with a water (H_2O) mass fraction lower than 50% (refs. [22-24]).

We analyse here eight transits of K2-18 b, obtained with the WFC3 camera on board the HST. We used our publicly available tools, specialized for HST/WFC3 data[5,9], to perform the end-to-end analysis from the raw data to the atmospheric parameters. The techniques used here have been validated by the analysis of the largest catalogue of exoplanetary spectra from WFC3[5]. Details can be found in Methods, and links to the data and the codes used can be found in 'Data availability' and 'Code availability', respectively. Along with the data, we provide descriptions of the data structures and instructions on how to reproduce the results presented here. Our analysis resulted in the detection of an atmosphere around K2-18 b with an Atmospheric Detectability Index[5] (ADI; a positively defined logarithmic Bayes factor) of 5.0, or approximately 3.6σ confidence[8,9], making K2-18 b the first habitable-zone planet in the super-Earth mass regime (1–10 $M_\oplus$) with an observed atmosphere around it.

More specifically, nine transits of K2-18 b were observed as part of the HST proposals 13665 and 14682 (principal investigator: Björn Benneke), and the data are available through the Mikulski Archive for Space Telescopes (MAST; see 'Data availability'). Each transit was observed during five HST orbits, with the G141 infrared grism (1.1–1.7 μm), and each exposure was the result of 16 up-the-ramp samples in the spatial scanning mode. The ninth transit observation suffered from pointing instabilities, and we therefore decided not to include it in this analysis. We extracted the white and the spectral light curves from the reduced images, following our dedicated methodology[5,17,25], which has been integrated into an automated, self-consistent and user-friendly Python package named Iraclis (see 'Code availability'). No systematic variations of the white light curve, $R_p/R_\star$, appeared between the eight different observations. This level of stability among the extracted broadband transit depths is not always guaranteed, as consistency problems among different observations emerged in previous analyses[5,16].

In our analysis, we found that the measured mid-transit times were not consistent with the expected ephemeris[19]. We used these results to refine the ephemeris of K2-18 b to be P = 32.94007 ± 0.00003 days and T_0 = 2457363.2109 ± 0.0004 BJD$_{TDB}$ (ref. [26]), where P

Department of Physics & Astronomy, University College London, London, UK. *e-mail: atsiaras@star.ucl.ac.uk; ingo@star.ucl.ac.uk

Table 1 | Transit depth $((R_p/R_\star)^2)$ for the different wavelength channels, where λ_1, λ_2 are the lower and upper edge of each wavelength channel, respectively
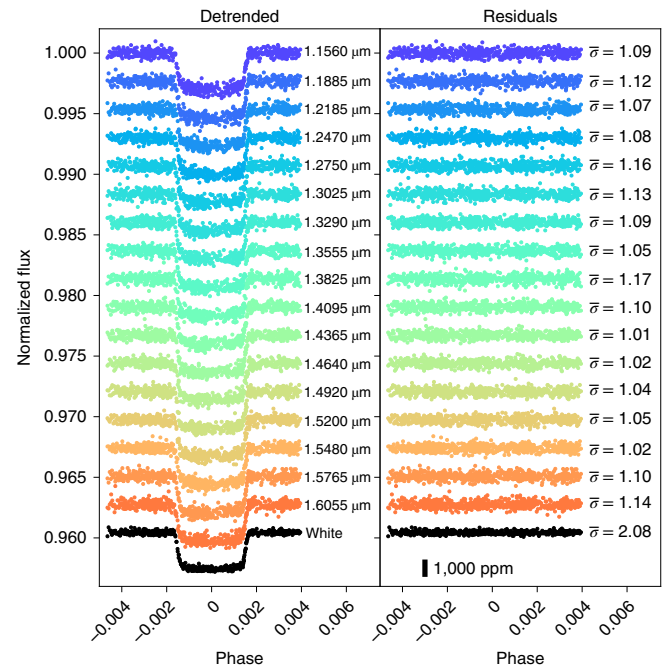
λ_1 (μm)	λ_2 (μm)	$(R_p/R_\star)^2$ (ppm)
1.1390	1.1730	2,905 ± 25
1.1730	1.2040	2,939 ± 26
1.2040	1.2330	2,903 ± 24
1.2330	1.2610	2,922 ± 25
1.2610	1.2890	2,891 ± 26
1.2890	1.3160	2,918 ± 26
1.3160	1.3420	2,919 ± 24
1.3420	1.3690	2,965 ± 24
1.3690	1.3960	2,955 ± 27
1.3960	1.4230	2,976 ± 25
1.4230	1.4500	2,990 ± 24
1.4500	1.4780	2,895 ± 23
1.4780	1.5060	2,930 ± 23
1.5060	1.5340	2,921 ± 24
1.5340	1.5620	2,875 ± 24
1.5620	1.5910	2,927 ± 25
1.5910	1.6200	2,925 ± 24

Fig. 1 | Analysis of the K2-18 b white and spectral light curves, plotted with an offset for clarity. Left: overplotted detrended white (black points) and spectral (coloured points) light curves. Right: overplotted fitted residuals, where $\bar{\sigma}$ indicates the ratio between the standard deviation of the residuals and the photon noise (see Methods for more details). The black vertical bar indicates the 1,000 ppm scatter level.

is the period, T_0 is the mid-time of the transit and BJD_{TDB} is the barycentric Julian date in the barycentric dynamical time standard. However, the ephemeris calculated only from the HST data is not consistent with the original detection of K2-18 b. One possibility is that the very sparse data from K2 are not sufficient to give a confident result. Another possibility is that we observe notable transit time variations (TTVs) caused by the other planet in the system, K2-18 c[22], but more observations over a long period of time are necessary to disentangle the two scenarios. In addition, we used the detrended and time-aligned—that is, with TTVs removed—white light curves to also refine the orbital parameters and found them to be $a/R_\star = 81.3 \pm 1.5$ and $i = 89.56 \pm 0.02$ deg, where $a/R_\star$ is the orbital semi-major axis normalized to the stellar radius and i is the orbital inclination.
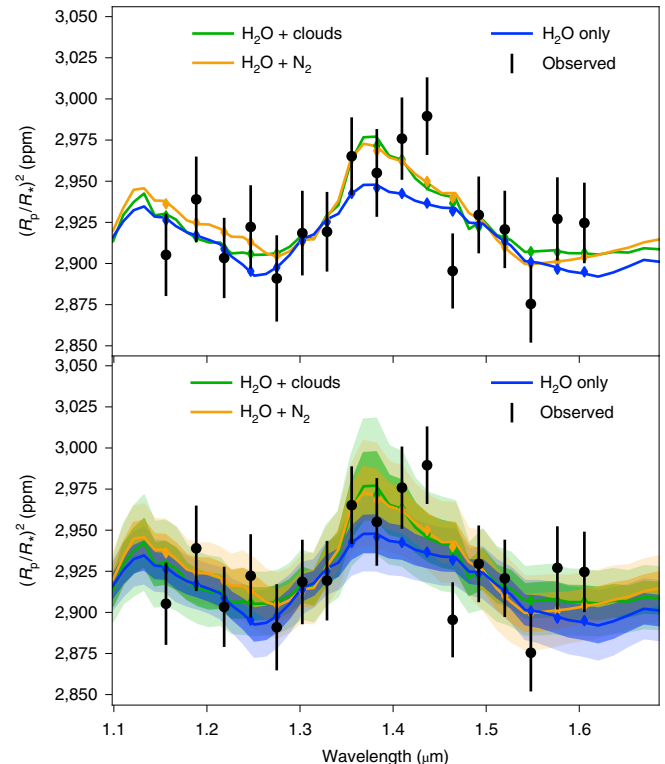
We extracted eight transmission spectra of K2-18 b and combined them, using a weighted average, to produce the final spectrum (Table 1). We interpreted the planetary spectrum using our spectral retrieval algorithm Tau-REx[9,27] (Tau Retrieval for Exoplanets; see 'Code availability'), which combines highly accurate line lists[28] (see 'Data availability') and Bayesian analysis. At an initial stage, we modelled the atmosphere of K2-18 b including all potential absorbers in the observed wavelength range, that is, H_2O, carbon monoxide (CO), carbon dioxide (CO_2), methane (CH_4) and ammonia (NH_3). However, we found that only the spectroscopic signature of water vapour is detected with high confidence, so we continued our analysis with only this molecule as trace gas. We modelled the atmosphere following three approaches:

- a cloud-free atmosphere containing only H_2O and H_2–He
- a cloud-free atmosphere containing H_2O, H_2–He and molecular nitrogen (N_2, which acted as proxy for 'invisible' molecules not detectable in the WFC3 bandpass but contributing to the mean molecular weight)
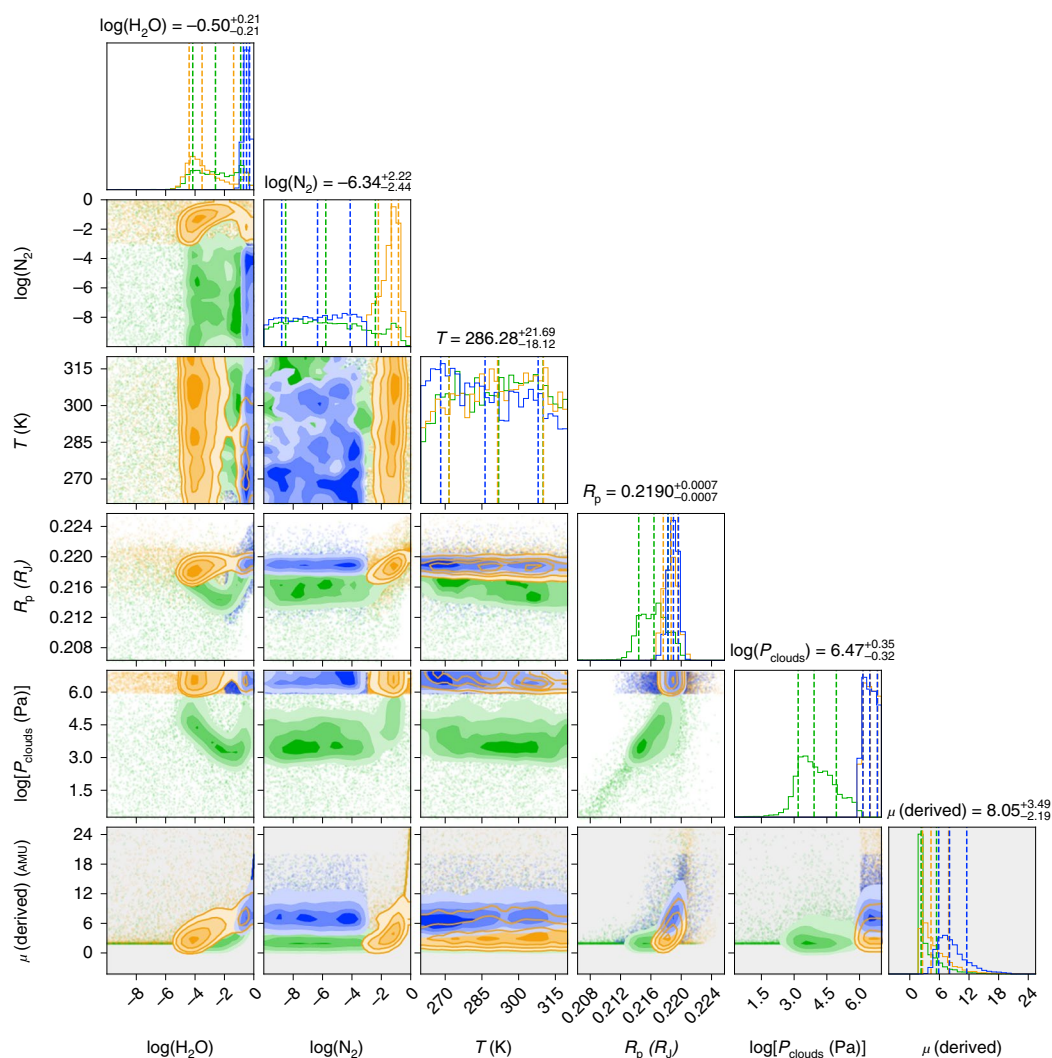- a cloudy (flat-line model) atmosphere containing only H_2O and H_2–He.

We retrieved a statistically significant atmosphere around K2-18 b in all simulations (Figs. 1–3), and assessed the strength of the

Fig. 2 | Best-fit models for the three different scenarios tested. A cloud-free atmosphere containing only H_2O and H_2–He (blue), a cloud-free atmosphere containing H_2O, H_2–He and N_2 (orange) and a cloudy atmosphere containing only H_2O and H_2–He (green). Top: best-fit models only. Bottom: 1σ and 2σ uncertainty ranges.

Fig. 3 | Posterior distributions for the three different scenarios tested. A cloud-free atmosphere containing only H_2O and H_2–He (blue), a cloud-free atmosphere containing H_2O, H_2–He and N_2 (orange), and a cloudy atmosphere containing only H_2O and H_2–He (green). From top to bottom: the volume mixing ratio of H_2O, $\log(H_2O)$; the volume mixing ratio of N_2, $\log(N_2)$; the planetary temperature, T, in K; the planetary radius in Jupiter radii (R_J); the cloud top pressure, $\log(P_{clouds})$, in Pa; the derived mean molecular weight, μ, in AMU.

detection using the ADI[5], which represents the positively defined logarithmic Bayes factor, where the null hypothesis is a model that contains no active trace gases, Rayleigh scattering or collision-induced absorption—that is, a flat spectrum. The retrieval simulations yield an atmospheric detection with ADI values of 5.0, 4.7 and 4.0, respectively. Such ADI values correspond to a detection of approximately 3.6σ, 3.5σ and 3.3σ (refs. [8,9]), respectively. This marks the first atmosphere detected around a habitable-zone super-Earth with such a high level of confidence. Although the $H_2O + H_2$–He case appears to be the most favourable, this preference is not statistically significant.

Concerning the composition, retrieval models confirm the presence of water vapour in the atmosphere of K2-18 b in all of the cases studied with high statistical significance. However, it is not possible to constrain either its abundance or the mean molecular weight of the atmosphere. For the $H_2O + H_2$–He case, we found the abundance of H_2O to be between 50% and 20%, while for the other two cases, it was between 0.01% and 12.5%. The atmospheric mean molecular weight can be between 5.8 AMU and 11.5 AMU in the $H_2O + H_2$–He case, and between 2.3 AMU and 7.8 AMU for the other cases. These results indicate that a non-negligible fraction of

the atmosphere is still made of H_2–He. Additional trace gases—for example, CH_4, NH_3—cannot be excluded, despite not being identified with the current observations: the limiting signal-to-noise ratio and wavelength coverage of HST/WFC3 do not allow the detection of other molecules.

The results presented here confirm the existence of a detectable atmosphere around K2-18 b, making it one of the most interesting known targets for further atmospheric characterization with future observatories such as the James Webb Space Telescope (0.6 μm and 28 μm) and the European Space Agency's ARIEL (Atmospheric Remote-sensing Infrared Exoplanet Large survey) mission[29] (0.5 μm and 7.8 μm). The wider wavelength coverage of these instruments will provide information on the presence of additional molecular species and on the temperature–pressure profile of the planet, towards studying the planetary climate and potential habitability. Although the subject of habitability for temperate planets around late-type stars is a subject of active discussion[10–13], and real progress requires substantially improved observational constraints, the analysis presented here provides the first direct observation of a molecular signature from a habitable-zone exoplanet, connecting these theoretical studies to observations.

Methods

Observations. Nine transits of K2-18 b were observed as part of the HST proposals 13665 and 14682 (principal investigator: Björn Benneke), and the data are available through the MAST. More specifically, the relevant HST visits are: visit 29 (06/12/2015), visit 35 (14/03/2016) and visit 30 (19/05/2016) from proposal 13665; visit 3 (02/12/2016), visit 1 (04/01/2017), visit 2 (06/02/2017), visit 4 (13/04/2017), visit 5 (30/11/2017) and visit 6 (13/05/2018) from proposal 14682. Out of these nine visits, we decided not to include the last one, as it suffered from pointing instabilities.

Each transit was observed during five HST orbits, with the G141 infrared grism of the WFC3 camera (1.1–1.7 μm), in the spatial scanning mode. During an exposure using the spatial scanning mode, the instrument slews along the cross-dispersion direction, allowing for longer exposure times and increased signal-to-noise ratio, without the risk of saturation[14]. Both forward (increasing row number) and reverse (decreasing row number) scanning were used for these observations.

The detector settings were SUBTYPE = SQ256SUB, SAMP_SEQ = SPARS10, NSAMP = 16, APERTURE = GRISM256, and the scanning speed was 1.4″ s^{-1}. The final images had a total exposure time of 103.128586 s, a maximum signal level of 1.9×10^4 electrons per pixel and a total scanning length of approximately 120 pixels. Finally, for calibration reasons, a 0.833445 s non-dispersed (direct) image of the target was taken at the beginning of each visit, using the F130N filter and the following settings: SUBTYPE = SQ256SUB, SAMP_SEQ = RAPID, NSAMP = 4, APERTURE = IRSUB256.

Extracting the planetary spectrum. We carried out the analysis of the eight K2-18 b transits using our specialized software for the analysis of WFC3 spatially scanned spectroscopic images[5,17,25], which have been integrated into the Iraclis package (see 'Code availability'). The reduction process included the following steps: zero-read subtraction, reference-pixels correction, nonlinearity correction, dark current subtraction, gain conversion, sky background subtraction, calibration, flat-field correction and bad-pixels/cosmic-rays correction.

We extracted the white (1.088–1.68 μm) and the spectral (Supplementary Table 1) light curves from the reduced images, taking into account the geometric distortions caused by the tilted detector of the WFC3 infrared channel[25]. The wavelength range of the white light curve corresponds to the edges of the WFC3/G141 throughput (where the throughput drops to 30% of the maximum). In addition, we tested two wavelength grids for the spectral light curves, with resolving powers of 20 and 50. We decided to use the latter as it was able to capture the observed water feature more precisely—that is, there were enough data points within the wavelength range of the water feature to produce a statistically significant result.

We fitted the light curves using our transit model package PyLightcurve, the transit parameters shown in Supplementary Table 2 and limb-darkening coefficients (Supplementary Table 1) calculated based on the PHOENIX[30] model, the nonlinear formula[31] and the stellar parameters in Supplementary Table 2.

More specifically, we fitted the white light curves with a transit model (with the planet-to-star radius ratio and the mid-transit time being the only free parameters) along with a model for the systematics[15,25]. It is common for WFC3 exoplanet observations to be affected by two kinds of time-dependent systematics[32–35]: the long-term and short-term 'ramps'. The first affects each HST visit and has a linear behaviour, while the second affects each HST orbit and has an exponential behaviour. The formula we used for the white light curve systematics (R_w) was the following:

$$R_w(t) = n_w^{scan}(1 - r_a(t - T_0))(1 - r_{b1}e^{-r_{b2}(t-t_o)}) \qquad (1)$$

where t is time, n_w^{scan} is a normalization factor, T_0 is the mid-transit time, t_o is the time when each HST orbit starts, r_a is the slope of a linear systematic trend along each HST visit and (r_{b1}, r_{b2}) are the coefficients of an exponential systematic trend along each HST orbit. The normalization factor we used (n_w^{scan}) was changed to n_w^{for} for upward scanning directions (forward scanning) and to n_w^{rev} for downward scanning directions (reverse scanning). The reason for using different normalization factors is the slightly different effective exposure time due to the known upstream/downstream effect[36]. We also varied the parameters of the orbit-long exponential ramp for the first orbit in the analysed time series (for$_{b1}$, for$_{b2}$ instead of r_{b1}, r_{b2}), because in many other HST observations, the first orbit was affected in a different way than the other orbits[5]. Although we used different ramp parameters from visit to visit, they appear to be consistent, which is an expected behaviour as the number of electrons collected per pixel per second is also consistent.

At the first stage, we fitted the white light curves using the formulae above and the uncertainties per pixel, as propagated through the data reduction process. However, it is common in HST/WFC3 data to have additional scatter that cannot be explained by the ramp model. For this reason, we scaled up the uncertainties in the individual data points, for their median to match the standard deviation of the residuals, and repeated the fitting[5]. From this second step of analysis, we found that the measured mid-transit times were not consistent with the expected ephemeris[19], which we found to be $P = 32.94007 \pm 0.00003$ days and $T_0 = 2457363.2109 \pm 0.0004$ BJD$_{TDB}$ (ref. [26]). Supplementary Fig. 1 shows

the difference between the predicted and the observed transit times using the ephemeris in the literature[19] and the one calculated in this work. We used the detrended and time-aligned—that is, with TTVs removed—white light curves to also refine the orbital parameters ($a/R_\star = 81.3 \pm 1.5$ and $i = 89.56 \pm 0.02$ deg). At the final step, we used all of the new parameters (ephemeris, and orbital parameters) to perform a final fit on the white light curves (again with the planet-to-star radius ratio and the mid-transit time being the only free parameters).

Supplementary Fig. 2 shows the raw white light curves, the detrended white light curves and the fitting residuals, as well as a number of diagnostics, while Supplementary Table 3 presents the fitting results. From these, we can see that

- the final planet-to-star radius ratio is consistent among the eight different transits, demonstrating the stability of both the instrument and the analysis process
- on average, the white light curve residuals show an autocorrelation of 0.17, which is a low number relative to the currently published observations of transiting exoplanets with HST[5] (up to 0.7), indicating a good fit
- uncorrected systematics are still present in the residuals, which, on average, show a scatter two times larger than the expected photon noise
- this extra noise component is taken into account by the increased uncertainties, as the reduced χ^2 is, on average, 1.16.

Furthermore, we fitted the spectral light curves with a transit model (with the planet-to-star radius ratio being the only free parameter) along with a model for the systematics (R_λ) that included the white light curve (divide-white method[15]) and a wavelength-dependent, visit-long slope[25]:

$$R_\lambda(t) = n_\lambda^{scan}(1 - \chi_\lambda(t - T_0))\frac{LC_w}{M_w} \qquad (2)$$

where χ_λ is the slope of a wavelength-dependent linear systematic trend along each HST visit, LC_w is the white light curve and M_w is the best-fit model for the white light curve. Again, the normalization factor we used (n_λ^{scan}) was changed to n_λ^{for} for upward scanning directions (forward scanning) and to n_λ^{rev} for downward scanning directions (reverse scanning). Also, in the same way as for the white light curves, we performed an initial fit using the pipeline uncertainties and then refitted while scaling these uncertainties up, for their median to match the standard deviation of the residuals.

Supplementary Figs. 3–19 show the raw spectral light curves, the detrended spectral light curves and the fitting residuals, as well as a number of diagnostics, while Supplementary Table 4 presents all the fitting results and average diagnostics per spectral channel. From these, we can see that

- the spectral light curves residuals show, on average, standard deviations much closer to the photon noise and lower values of autocorrelation, proving the advantage of using the white light curve as a model over the ramp model
- any extra noise component is taken into account by the scaled-up uncertainties, as the reduced χ^2 is for all channels, on average, close to 1.

Finally, the eight spectra of K2-18 b (Supplementary Fig. 20) were combined, using a weighted average, to produce the final spectrum (Table 1).

Stellar contamination. K2-18 is a moderately active M2.5V star, with a variability of 1.7% in the B band and 1.38% in the R band[37]. Hence, to make sure that the observed water feature is not the effect of stellar contamination, we fitted the observed spectrum with a model that assumes a flat planetary spectrum and contribution only from the star (M2V star as described in Rackham et al.[38]). The model that best describes our data has a spot coverage of 26% and a faculae coverage of 73%. We plot this spectrum versus the observed one in Supplementary Fig. 21. In addition, we plot the spectrum produced by the spot and faculae combination reported by Rackham et al.[38] and corresponding to a 1% I-band variability, for reference. However, as Supplementary Fig. 21 shows, the best-fit model cannot describe the observed water feature. We therefore conclude that there is no combination of stellar properties that could introduce the observed water feature.

Atmospheric retrieval. We fitted the final planetary spectrum using our Bayesian atmospheric retrieval framework Tau-REx[9,27], which fully maps the correlations between the fitted atmospheric parameters through nested sampling[39,40].

The atmosphere of K2-18 b was simulated as a plane-parallel atmosphere with pressures ranging from 10^{-4} Pa to 10^6 Pa, sampled uniformly in log space by 100 atmospheric layers, assuming an isothermal temperature–pressure profile. We initially tested fitting for a number of trace gases—H_2O (ref. [41]), CO (ref. [42]), CO_2 (ref. [42]), CH_4 (ref. [43]) and NH_3 (ref. [44])—but found that only water vapour plays a substantial role. Hence, we proceeded with only this molecule. We also included the effect of clouds using a grey/flat-line model, as the quality and wavelength ranges of the currently available observations do not allow us to make any reasonable constraints on the haze properties of the planet. Finally, we included the spectroscopically inactive N_2 as an inactive gas, to account for any unseen absorbers—for example, methane, which is expected at these temperatures. As free parameters in our models, we had the volume mixing ratio of H_2O (log-uniform prior between 10^{-10} and 1.0), the volume mixing ratio of N_2 (log-uniform prior between 10^{-10} and 1.0), the planetary temperature (uniform prior between 260 K and 320 K), the planetary radius (uniform prior

between 0.05 Jupiter radii (R_J) and 0.5 R_J) and the cloud top pressure (log-uniform prior between 10^{-3} Pa and 10^7 Pa, where 10^7 Pa represents a cloud-free atmosphere). We restricted the temperature prior compared with all the possible temperatures for different values of albedo and emissivity because, since we can detect only water, the temperature of the atmospheric part probed must be higher than the freezing point of water (~260 K at 1 mbar).

We identified three solutions: (1) a cloud-free atmosphere containing only H_2O and H_2–He, (2) a cloud-free atmosphere containing H_2O, H_2–He and N_2 and (3) a cloudy atmosphere containing only H_2O and H_2–He. The best-fit spectra and the posterior plots[45] are shown in Fig. 3. In all cases, a statistically significant atmosphere around K2-18 b was retrieved with ADIs[5] of 5.0, 4.7 and 4.0, respectively. An ADI of 5 corresponds approximately to a 3.6σ (refs. [8,9]) detection of an atmosphere. The values are too similar to distinguish between the three scenarios.

Data availability

The data analysed in this work are available through the NASA MAST HST archive (https://archive.stsci.edu/) programmes 13665 and 14682. The molecular line lists used are available from the ExoMol website (www.exomol.com). The final and intermediate results (reduced data, extracted light curves, light curve fitting results and atmospheric fitting results) are available through the University College London Exoplanets website (https://www.ucl.ac.uk/exoplanets) and the Open Science Framework (OSF) website at https://doi.org/10.17605/OSF.IO/N7DQX.

Code availability

All the software used to produce the presented results are publicly available through the University College London Exoplanets GitHub website (https://github.com/ucl-exoplanets/). More specifically, the codes used were Tau-REx (https://github.com/ucl-exoplanets/TauREx_public), Iraclis (https://github.com/ucl-exoplanets/Iraclis) and PyLightcurve (https://github.com/ucl-exoplanets/pylightcurve).

References

1. Tinetti, G. et al. Infrared transmission spectra for extrasolar giant planets. *Astrophys. J. Lett.* **654**, L99–L102 (2007).
2. Grillmair, C. J. et al. Strong water absorption in the dayside emission spectrum of the planet HD189733b. *Nature* **456**, 767–769 (2008).
3. Fraine, J. et al. Water vapour absorption in the clear atmosphere of a Neptune-sized exoplanet. *Nature* **350**, 64–67 (2015).
4. Macintosh, B. et al. Discovery and spectroscopy of the young jovian planet 51 Eri b with the Gemini Planet Imager. *Science* **456**, 767–769 (2008).
5. Tsiaras, A. et al. A population study of gaseous exoplanets. *Astron. J.* **155**, 156 (2018).
6. de Wit, J. et al. Atmospheric reconnaissance of the habitable-zone Earth-sized planets orbiting TRAPPIST-1. *Nat. Astron.* **2**, 214–219 (2018).
7. Montet, B. T. et al. Stellar and planetary properties of K2 Campaign 1 candidates and validation of 17 planets, including a planet receiving Earth-like insolation. *Astrophys. J.* **809**, 25 (2015).
8. Benneke, B. & Seager, S. How to distinguish between cloudy mini-Neptunes and water/volatile-dominated super-Earths. *Astrophys. J.* **778**, 153 (2013).
9. Waldmann, I. P. et al. Tau-REx I: a next generation retrieval code for exoplanetary atmospheres. *Astrophys. J.* **802**, 107 (2015).
10. Segura, A. et al. Biosignatures from Earth-like planets around M dwarfs. *Astrobiology* **5**, 706–725 (2005).
11. Wordsworth, R. D. et al. Gliese 581d is the first discovered terrestrial-mass exoplanet in the habitable zone. *Astrophys. J.* **733**, L48 (2011).
12. Leconte, J. et al. 3D climate modeling of close-in land planets: circulation patterns, climate moist bistability, and habitability. *Astron. Astrophys.* **554**, A69 (2013).
13. Turbet, M. et al. The habitability of Proxima Centauri B. II. Possible climates and observability. *Astron. Astrophys.* **596**, A112 (2016).
14. Deming, D. et al. Infrared transmission spectroscopy of the exoplanets HD 209458b and XO-1b using the Wide Field Camera-3 on the Hubble Space Telescope. *Astrophys. J.* **774**, 95 (2013).
15. Kreidberg, L. et al. Clouds in the atmosphere of the super-Earth exoplanet GJ1214b. *Nature* **505**, 69–72 (2014).
16. Knutson, H. A. et al. Hubble Space Telescope near-IR transmission spectroscopy of the super-Earth HD 97658b. *Astrophys. J.* **794**, 155 (2014).
17. Tsiaras, A. et al. Detection of an atmosphere around the super-Earth 55 Cancri e. *Astrophys. J.* **820**, 99 (2016).
18. Wakeford, H. R. et al. Disentangling the planet from the star in late-type M dwarfs: a case study of TRAPPIST-1g. *Astron. J.* **157**, 11 (2019).
19. Benneke, B. et al. Spitzer observations confirm and rescue the habitable-zone super-Earth K2-18b for future characterization. *Astrophys. J.* **834**, 187 (2017).
20. Kopparapu, R. K. A revised estimate of the occurrence rate of terrestrial planets in the habitable zones around Kepler M-dwarfs. *Astrophys. J. Lett.* **767**, L8 (2013).
21. Valencia, D., Tan, V. Y. Y. & Zajac, Z. Habitability from tidally induced tectonics. *Astrophys. J.* **857**, 106 (2018).
22. Cloutier, R. et al. Characterization of the K2-18 multi-planetary system with HARPS. A habitable zone super-Earth and discovery of a second, warm super-Earth on a non-coplanar orbit. *Astron. Astrophys.* **608**, A35 (2017).
23. Valencia, D., Guillot, T., Parmentier, V. & Freedman, R. S. Bulk composition of GJ 1214b and other sub-Neptune exoplanets. *Astrophys. J.* **775**, 10 (2013).
24. Zeng, L., Sasselov, D. D. & Jacobsen, S. B. Mass–radius relation for rocky planets based on PREM. *Astrophys. J.* **819**, 127 (2016).
25. Tsiaras, A. et al. A new approach to analyzing HST spatial scans: the transmission spectrum of HD 209458 b. *Astrophys. J.* **832**, 202 (2016).
26. Eastman, J. et al. Achieving better than 1 minute accuracy in the heliocentric and barycentric Julian dates. *Publ. Astron. Soc. Pac.* **122**, 935 (2010).
27. Waldmann, I. P. et al. Tau-REx II: retrieval of emission spectra. *Astrophys. J.* **813**, 13 (2015).
28. Tennyson, J. et al. The ExoMol database: molecular line lists for exoplanet and other hot atmospheres. *J. Mol. Spec.* **327**, 73–94 (2016).
29. Tinetti, G. et al. A chemical survey of exoplanets with ARIEL. *Exp. Astron.* **46**, 135–209 (2018).
30. Allard, F., Homeier, D. & Freytag, B. Models of very-low-mass stars, brown dwarfs and exoplanets. *Philos. Trans. R. Soc. A* **370**, 2765–2777 (2012).
31. Claret, A. A new non-linear limb-darkening law for LTE stellar atmosphere models. Calculations for $-5.0 <= \log[M/H] <= +1, 2000\,K <= T_{eff} <= 50000\,K$ at several surface gravities. *Astron. Astrophys.* **363**, 1081–1190 (2000).
32. Kreidberg, L. et al. A detection of water in the transmission spectrum of the hot Jupiter WASP-12b and implications for its atmospheric composition. *Astrophys. J.* **814**, 66 (2015).
33. Evans, T. M. et al. Detection of H_2O and evidence for TiO/VO in an ultra-hot exoplanet atmosphere. *Astrophys. J. Lett.* **822**, L4 (2016).
34. Line, M. R. et al. No thermal inversion and a solar water abundance for the hot Jupiter HD 209458b from HST/WFC3 spectroscopy. *Astron. J.* **152**, 203 (2016).
35. Wakeford, H. R. et al. HST PanCET program: a cloudy atmosphere for the promising JWST target WASP-101b. *Astrophys. J. Lett.* **835**, L12 (2017).
36. McCullough, P. & MacKenty, J. *Considerations for Using Spatial Scans with WFC3* Instrument Science Report WFC3 2012-08 (STSI, 2012).
37. Sarkis, P. et al. The CARMENES search for exoplanets around M dwarfs: a low-mass planet in the temperate zone of the nearby K2-18. *Astron. J.* **155**, 257 (2018).
38. Rackham, B. V., Apai, D. & Giampapa, M. S. The transit light source effect: false spectral features and incorrect densities for M-dwarf transiting planets. *Astrophys. J.* **853**, 122 (2018).
39. Skilling, J. Nested sampling for general Bayesian computation. *Bayesian Anal.* **1**, 833–860 (2006).
40. Feroz, F., Hobson, M. P. & Bridges, M. MULTINEST: an efficient and robust Bayesian inference tool for cosmology and particle physics. *Mon. Not. R. Astron. Soc.* **398**, 1601–1614 (2009).
41. Barber, R. J., Tennyson, J., Harris, G. J. & Tolchenov, R. N. A high-accuracy computed water line list. *Mon. Not. R. Astron. Soc.* **368**, 1087–1094 (2006).
42. Rothman, L. S. et al. HITEMP, the high-temperature molecular spectroscopic database. *J. Quant. Spec. Rad. Transf.* **111**, 2139–2150 (2010).
43. Yurchenko, S. N. & Tennyson, J. ExoMol line lists—IV. the rotation–vibration spectrum of methane up to 1500 K. *Mon. Not. R. Astron. Soc.* **440**, 1649–1661 (2014).
44. Yurchenko, S. N., Barber, R. J. & Tennyson, J. A variationally computed line list for hot NH_3. *Mon. Not. R. Astron. Soc.* **413**, 1828–1834 (2011).
45. Foreman-Mackey, D. corner.py: scatterplot matrices in Python. *J. Open Source Softw.* **24**, 1 (2016).

Author contributions

A.T. performed the data analysis and developed the HST analysis software Iraclis; I.P.W. developed the atmospheric retrieval software Tau-REx; G.T. contributed to the interpretation of the results; J.T. and S.N.Y. coordinated the ExoMol project. All authors discussed the results and commented on the manuscript.

Competing interests

The authors declare no competing interests.

Additional information

Supplementary information is available for this paper at https://doi.org/10.1038/s41550-019-0878-9.

Reprints and permissions information is available at www.nature.com/reprints.